engineering proceedings

MDPI

Proceeding Paper

Investigation on Gaseous Cavitation Characteristics of Fluid Supply System Pipelines †

Zhipeng Ren [1], Zhenbing Gu [2], Yuxin Zhong [1], Zhiyuan Zhang [1], Zhenjian Jia [3], Lingcong Nie [2] and Weixing Zhou [1,3,*]

[1] School of Energy Science and Engineering, Harbin Institute of Technology, Harbin 150001, China; renzhipeng@hit.edu.cn (Z.R.); zhongyuxinhit@163.com (Y.Z.); zhangzhiyuan__hit@163.com (Z.Z.)
[2] Beijing Power Machinery Research Institute, Beijing 100074, China; sylgok@126.com (Z.G.); nielingcong@163.com (L.N.)
[3] Harbin Institute of Technology Zhengzhou Advanced Research Institute, Zhengzhou 450000, China; jiahcms@163.com
* Correspondence: zhouweixing@hit.edu.cn
† Presented at the 8th International Conference on Nuclear and Renewable Energy Resources (NURER 2026), Almaty, Kazakhstan, 10–12 September 2026.

Abstract

The throttling effect of variable-diameter sections in fluid supply pipelines causes abrupt local pressure drop and temperature variation, leading to explosive precipitation of dissolved gas in fuel, seriously compromising fuel supply stability, combustion performance and thermal management system reliability. Accordingly, this study adopts an improved gaseous cavitation model to conduct numerical simulation on gaseous cavitation behavior in pipelines. After completing grid independence verification and experimental validation, the spatial distribution characteristics of bubble size under gas-containing conditions are firstly investigated. Furthermore, the gas–liquid distribution behavior under variable flow rate conditions is analyzed to identify gas accumulation locations. Finally, unsteady numerical simulations are carried out for typical operating conditions to clarify the temporal and spatial evolution characteristics of phase separation and abrupt mass-transfer direction. The formation mechanism of gaseous cavitation flow in fuel supply pipelines is ultimately elucidated. The findings of this research can provide theoretical support for the investigation and control of flow instability in engine fuel supply systems.

Keywords: fuel supply system; gaseous cavitation; pipeline system; gas–liquid behavior; mass-transfer characteristics

1. Introduction

The demand for high-pressure circulating recirculation technology is a key requirement for equipment hydraulic transmission and lubrication systems, and it is widely applied in nuclear engineering [1–3], hydraulic engineering [4,5], and aerospace engineering [6,7]. This requirement focuses on the pressure resistance and dynamic response characteristics of circulation circuits under extreme operating conditions. On the one hand, it is necessary to ensure that the circulation circuit and its valves can maintain structural integrity and sealing performance under high-frequency pressure shocks and pressure fluctuations, and avoid pipeline rupture and joint leakage caused by peak pressure. On the other hand, when the system is subjected to rapid temperature changes, the circulation circuit needs to adapt to medium recirculation with a wide temperature range

Check for updates

Academic Editors: Sümer Şahin, Hacı Mehmet Şahin and Bekir Dursun

Published: 22 October 2026

Copyright: © 2026 by the authors. Licensee MDPI, Basel, Switzerland. This article is an open access article distributed under the terms and conditions of the Creative Commons Attribution (CC BY) license.

and variable viscosity, so as to prevent abnormal back pressure, system response delay and gaseous cavitation caused by differences in fluidity. Meanwhile, it is essential to clarify the transport and collapse mechanism of bubbles under high-pressure recirculation conditions, so as to optimize the flow channel design and mitigate cavitation erosion damage to pipeline walls and components.

Mass transfer between gas and liquid phases exists in numerous fields such as wastewater treatment, architectural design and ecological environment, which can be regarded as a multi-phase component transport process [8–11]. Due to the influences of physical parameters, hydrodynamic characteristics and chemical reactions, the properties of dissolved and precipitated gases are highly complex and diverse. During the gas–liquid mass-transfer process, dynamic mass-transfer equilibrium is achieved when the dissolved gas reaches its equilibrium solubility under specific temperature and pressure conditions [12,13]. Numerical simulation has become one of the key approaches to investigate the dynamic characteristics of gas dissolution and precipitation.

Focusing on the unidirectional dissolution process, Li et al. [14] proposed a reliable prediction method for mass-transfer coefficients applicable to mass transfer inside bubbles. Long et al. [15] adopted the Euler–Euler method to describe gas–liquid flow in bubble columns. Huang et al. [16] and Yan et al. [17] carried out computational fluid dynamics simulations on mass-transfer characteristics in bubble columns based on the two-film theory. Zhou [18] employed a multi-size bubble group model to explore the temporal and spatial evolution of dissolved oxygen in bubble reactors. The results indicated that steady and pulsating gas flow rates significantly affect the mass-transfer coefficient, and the pulsation frequency exhibits a negative linear correlation with the mass-transfer coefficient. Nevertheless, compared with corresponding experimental data, the maximum error of mass-transfer coefficients in these numerical studies can reach up to 30%. Based on the experimental results of Zhou et al. [18], Daskiran et al. [19] utilized the Higbie penetration theory to predict local bubble size and oxygen mass-transfer characteristics of ventilated rotating blades, and further extended this method to hydraulic turbine research [20].

The isothermal dissolution theory based on the two-film law and its derivative formulations is well-established, and numerical simulations and experimental studies have provided comprehensive insights into gas–liquid mass-transfer behavior. At present, most researchers focus on quasi-static gas dissolution and exsolution processes, while the understanding of dynamic gas–liquid mass transfer and fluid flow—especially the coupled effects of gas dissolution and exsolution—remains incomplete. In the research on flow instability in pumps, existing studies predominantly focus on single cavitation states, and the coupling mechanism between dynamic dissolution and exsolution processes has not yet been clarified. Therefore, this study develops a mathematical model for gas dissolution and exsolution mass transfer applicable to three-dimensional computations, enabling the coupling of independent unidirectional gas–liquid mass-transfer processes. The proposed model integrates the complete dynamic theories of both dissolution and exsolution. Referring to the definitions of evaporation and condensation in vapor cavitation models, the processes of gas dissolution and exsolution are formulated. Two practical cases, namely orifice flow and pipeline or plate flow, are adopted to verify the concentration characteristics in the flow domain and evaluate the prediction accuracy of the mass-transfer model. This work further reveals the interdependent relationship between gas–liquid flow regime transition and concentration variation in pipeline systems.

https://doi.org/10.3390/engproc2026160024

2. Numerical Strategy

2.1. Computational Model

In this study, ICEM 17.0 is adopted as the mesh generation software. Based on the geometric topological characteristics of the computational domain, a hexahedron-dominated strategy is applied to generate high-quality structured meshes, as shown in Figure 1. Meanwhile, a highly ordered mesh arrangement scheme is employed to fill the core computational region, which ensures computational accuracy and numerical stability while effectively controlling the total number of meshes.



(**a**) (**b**)

Figure 1. Hexahedral structured grid of the pipeline: (**a**) Mesh of pipeline variable-diameter section; (**b**) radial mesh distribution.

2.2. Gaseous Cavitation Model

The gaseous cavitation process is analogous to the vapor cavitation process [21,22]. Vapor cavitation generally consists of two stages: evaporation and condensation. Mass transfer between the vapor and liquid phases is governed by the mixture continuity equation and relevant transport equations [23]. Unlike vapor cavitation, the liquid phase in gaseous cavitation contains at least two components and exists as a mixture; therefore, a component transport model is required. Under constant ambient temperature, gaseous cavitation is pressure-dependent. According to Henry's law and Raoult's law, gaseous cavitation initiates when the local pressure drops below the equilibrium saturation pressure [24]. In accordance with Henry's law, the saturation pressure of dissolved gas is proportional to the mole fraction of the dissolved component at equilibrium, and the dissolved gas concentration under equilibrium conditions can be expressed as follows.

$$Y_{gas,eq} = \frac{P_{gas,g}}{He} \tag{1}$$

$x_{gas,eq}$ denotes the equilibrium mole fraction of dissolved oxygen in the liquid phase under equilibrium conditions; He is the Henry constant, and $P_{gas,g}$ represents the partial pressure of gas in the entire gas mixture. When the mass-transfer process is assumed to be isothermal, the fluid properties remain constant, and the Henry constant is kept unchanged.

$$R = \begin{cases} \frac{C_d}{\tau}\rho(Y_0 + \alpha_g\frac{\rho_g}{\rho} - Y)[|(p_s - p|]^{\frac{1}{2}} \ (Y \le Y_{gas,eq}) \\ -\frac{C_r}{\tau}\rho Y[|[p_s - p|]^{\frac{1}{2}} (Y > Y_{gas,eq}) \end{cases} \tag{2}$$

Y_0 and Y are the initial and current mass fractions of dissolved gas, respectively. The detailed derivation process can be referred to in Ref. [21].

2.3. Numerical Method and Boundary Conditions

The SST k–ω turbulence model and the Mixture multiphase model are adopted for the simulations to resolve the gas–liquid two-phase flow. The primary phase is defined as liquid with dissolved gas, and the secondary phase is defined as gas. In order to

ensure the accuracy of simulation calculation and the convergence of numerical simulation, geometric simplification is adopted on the basis of the actual structure. On the one hand, the rationality of the simulation results for practical physical problems can be guaranteed; on the other hand, computational resources can be saved and the convergence performance of the simulation can be improved. Therefore, in this study, the pipe wall of the cooling flow path is simplified as an adiabatic wall.

The boundary conditions are set as follows: (1) The inlet of the fuel–air mixture is set as a velocity inlet; (2) the air inlet is set as a velocity inlet; (3) and the outlet of the cooling oil passage is set as a pressure outlet.

The simplified structure of the computational model is shown in Figure 2, and the specific boundary condition parameters are listed in Table 1.

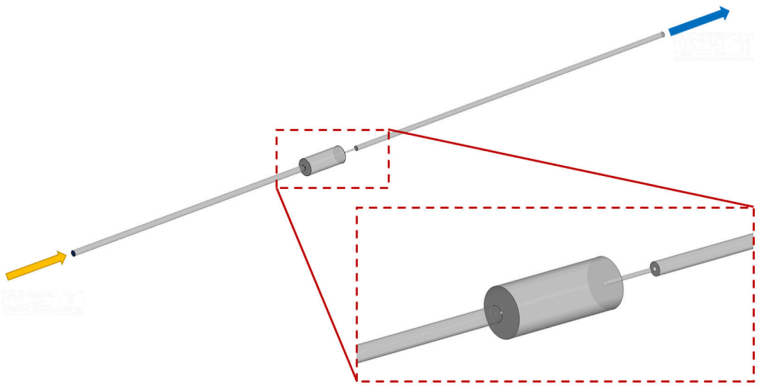


Figure 2. Simplified structure of fuel supply pipeline system.

Table 1. Calculation condition parameters.

Temperature (°C)	Inlet Flow Rate (kg/s)	Inlet Velocity (m/s)	Mass Fraction (-)	Back Pressure at (kPa)
150	0.02	0.88	7.92×10^{-6}	140
	0.06	2.63	5.81×10^{-5}	
	0.1	4.39	1.49×10^{-4}	

3. Results and Discussion

3.1. Validation of Experiments

Based on the research of Yin et al. [25], the dissolved oxygen concentration measured at point M1 was linearly fitted as the inlet boundary condition within 100 s. The dissolved oxygen concentration was calculated through numerical simulation. The ±2.0% error band of measured values is plotted in Figure 3. The prediction error of the concentration is less than 2%, and the numerical results show good agreement with the experimental data. It is demonstrated that the proposed gas dissolution and precipitation model has high accuracy.

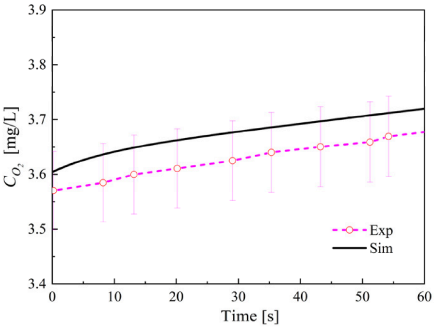


Figure 3. Comparison between experimental data [25] and numerical results.

3.2. Gaseous Cavitation Calculation of Pipeline

This study investigates the gas volume distribution of bubble groups with different sizes within the fuel passage of a high-temperature valve under various inlet velocities, including 0.884 m/s, 2.636 m/s and 4.394 m/s. The results show that the increase in inlet velocity promotes gas accumulation in the pipeline. At the inlet velocity of 4.394 m/s, the gas exhibits a discontinuous distribution inside the pipeline, presenting a pattern similar to that of linear cavitation regions, as illustrated in Figure 4. The red color denotes the isosurface of a gas phase volume fraction of 50%.

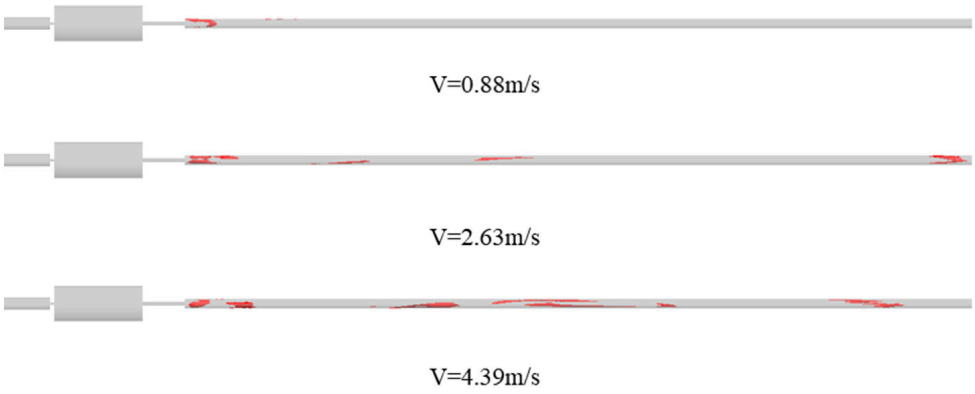


Figure 4. Fifty percent gas volume fraction isosurface.

The bubbles are divided into five groups with respective sizes of 0.030 mm, 0.023 mm, 0.017 mm, 0.013 mm, and 0.010 mm. Figures 5–7 illustrate the gas phase distribution within the computational domain under different operating conditions. The results show that, at an inlet velocity of 0.88 m/s and a bubble size of 0.030 mm, a high gas fraction distribution appears in the pipeline with a wide gas coverage area. Within the constricted section, the gas phase exhibits a prominent central peak distribution, where gas accumulates mainly in the central region of the constricted pipe, while the gas fraction near the wall remains low.

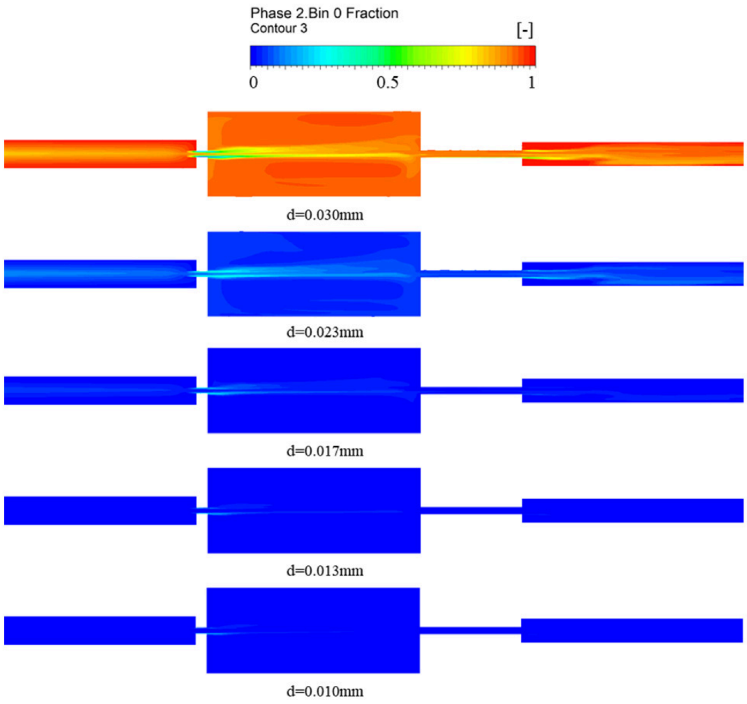


Figure 5. Cloud map of bubble distribution with different sizes in the computational domain under the inlet velocity of 0.88 m/s.

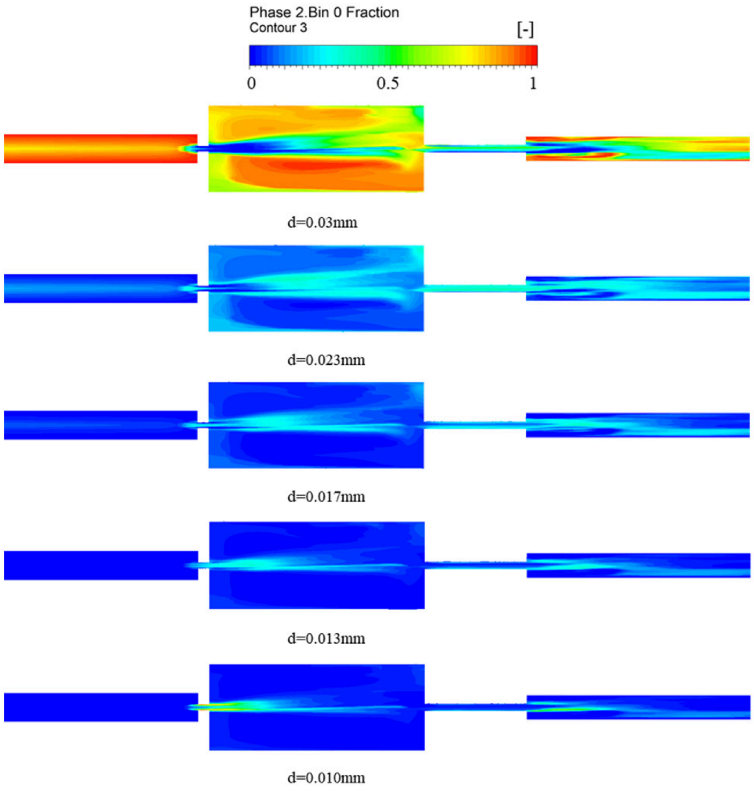


Figure 6. Cloud map of bubble distribution with different sizes in the computational domain under the inlet velocity of 2.63 m/s.

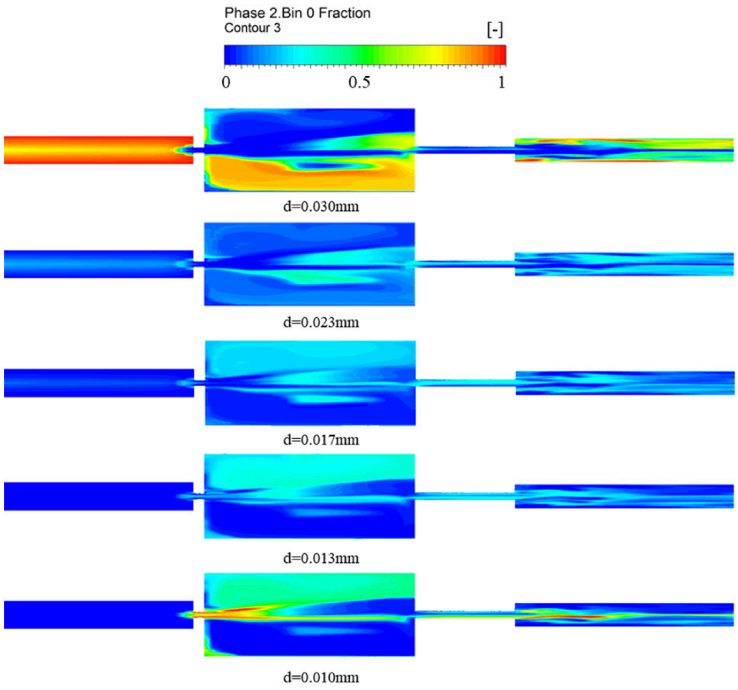


Figure 7. Cloud map of bubble distribution with different sizes in the computational domain under the inlet velocity of 4.39 m/s.

As the bubble size decreases gradually, the overall gas fraction in the flow field decreases significantly, leading to a low gas distribution state. In the constricted section, the gas phase tends to form a distinct wall peak distribution, with gas concentrating near the pipe wall, which is opposite to the distribution pattern of the 0.030 mm bubble group.

With the increase in inlet velocity, the gas fraction of all bubble groups in the pipeline rises significantly. At an inlet velocity of 2.63 m/s, the gas fraction increases for the bubble group of 0.010 mm, accompanied by an obvious rise in gas content at the outlet of the constricted section. When the inlet velocity increases to 4.3935 m/s, the gas fraction recovery of the 0.010 mm bubble group becomes remarkably enhanced.

3.3. Temporal and Spatial Evolution Characteristics of Gas–Liquid Distribution in the Pipeline

This study investigates the distribution of mass-transfer rate in the flow field under different inlet velocities. The mass-transfer rate characterizes the intensity of gas–liquid mass exchange in the fuel channel, and its temporal and spatial evolution directly reflects the development, attenuation and dynamic balance characteristics of the cavitation process. The inlet velocities adopted are 0.88 m/s, 2.63 m/s and 4.39 m/s, respectively. The contour maps of mass-transfer rate distribution in the computational domain at different time moments under each condition are shown in Figure 8.

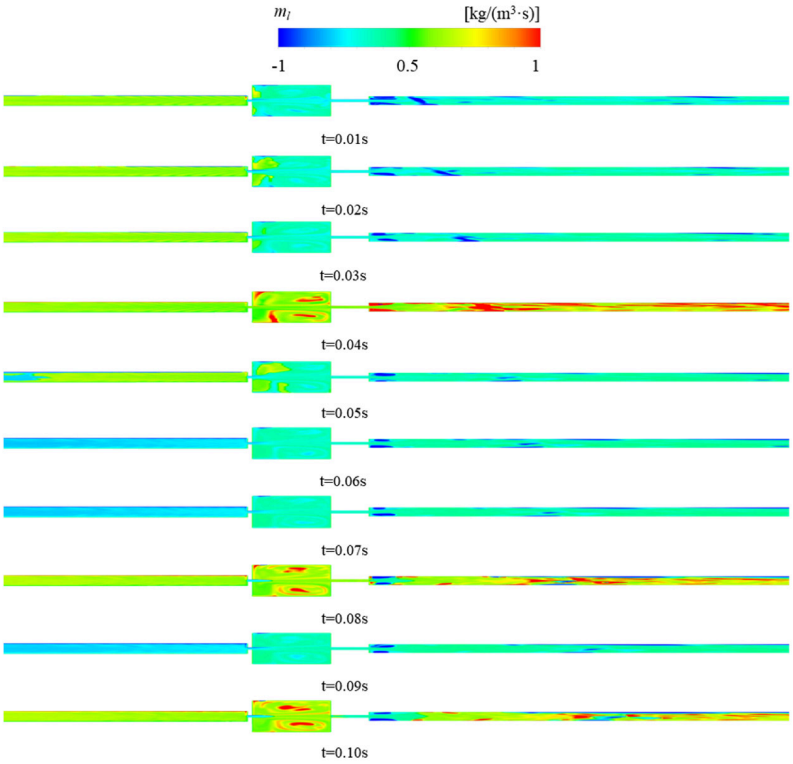


Figure 8. Cloud map of mass-transfer rate with different sizes in the computational domain under the inlet velocity of 0.88 m/s.

The results indicate that at an inlet velocity of 0.884 m/s, the mass-transfer rate remains at a low level and concentrates in the junction area between the inlet and the expanded section from t = 0.01 s to t = 0.03 s. Affected by abrupt geometric changes in the flow channel, local flow disturbances occur in this region, which becomes the initial active area of mass transfer with a narrow distribution range and insignificant fluctuation in magnitude. At t = 0.04 s, the enhancement of turbulent fluctuations strengthens the driving force for interfacial mass transfer, leading to a significant rise in the mass-transfer rate and the emergence of a global peak. The distribution range rapidly extends to the expanded section and the outlet section, representing the most active moment of mass transfer throughout the entire process. At t = 0.05 s, flow field disturbances gradually subside, the mass-transfer driving force declines sharply, the mass-transfer rate drops substantially, and the distribution range shrinks accordingly, returning to a low level similar to the initial state.

https://doi.org/10.3390/engproc2026160024

From t = 0.06 s to t = 0.10 s, the mass-transfer rate fluctuates slightly at a low value, and the active area remains confined to the junction of the inlet and expanded section without obvious expansion or migration.

At an inlet velocity of 2.636 m/s, the mass-transfer rate concentrates on the junction of the inlet and expanded section at t = 0.01 s. Due to the increased inlet kinetic energy, the initial mass-transfer rate is slightly higher than that of the low-velocity condition, while still maintaining an overall low level with a narrow distribution range. From t = 0.02 s to t = 0.04 s, the turbulent intensity in the flow channel continuously increases, the gas–liquid interfacial area gradually expands, and the mass-transfer rate rises steadily in a stepwise manner. Its distribution range extends toward the inlet section, and the mass-transfer activity increases continuously over time, reaching the peak value at t = 0.04 s. At t = 0.05 s, the flow field gradually approaches dynamic equilibrium, the interfacial mass exchange tends to stabilize, the mass-transfer rate decreases rapidly, and the distribution range contracts significantly. From t = 0.06 s to t = 0.08 s, the mass-transfer rate decreases slowly at a low level, and the active area is restricted to the core junction of the inlet and expanded section. The behavior from t = 0.09 s to t = 0.10 s is presented in Figure 9.

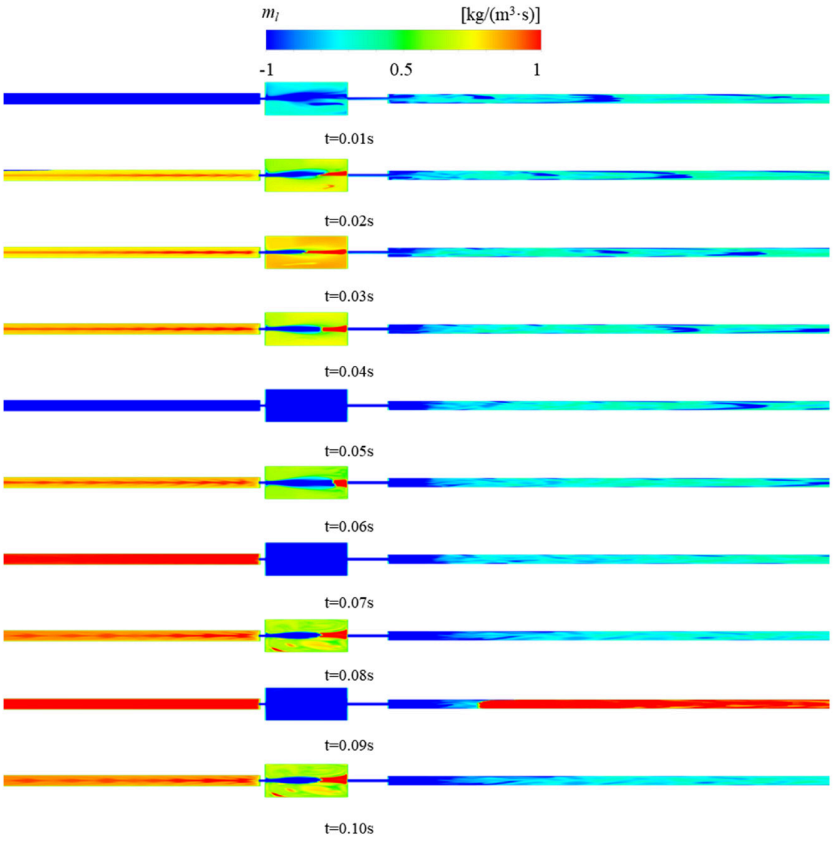


Figure 9. Cloud map of mass-transfer rate with different sizes in the computational domain under the inlet velocity of 2.63 m/s.

Under the high inlet velocity of 4.394 m/s, intense initial turbulent disturbances are generated in the flow channel. Accordingly, the mass-transfer rate is already at a relatively high level at t = 0.01 s, and the active area directly covers the junction from the inlet to the expanded section. The interfacial mass-transfer driving force is significantly higher than that of low and medium velocity conditions, resulting in the maximum initial mass-transfer intensity across all time points. From t = 0.02 s to t = 0.04 s, the mass-transfer rate remains at a high level with minor fluctuations and no distinct peak. Influenced by wall viscous dissipation and flow field rearrangement, the active area gradually contracts toward the

expanded section, and the mass-transfer intensity in the inlet section decreases gradually. At t = 0.05 s, turbulent energy dissipates, the driving force for gas–liquid mass-transfer weakens, the mass-transfer rate decreases obviously, and the active area further contracts to local regions of the expanded section. From t = 0.06 s to t = 0.07 s, the mass-transfer rate declines steadily with no obvious migration of the active area, which remains concentrated in the core of the expanded section. From t = 0.08 s to t = 0.10 s, the mass-transfer rate decreases to a medium–low level and tends to stabilize with negligible fluctuation, and the flow field enters a steady dynamic mass-transfer state.

Overall, the increase in inlet velocity elevates the initial mass-transfer rate and advances the onset of intense mass transfer. Under high-flow conditions, the mass-transfer peak becomes milder and lasts for a longer duration. The temporal and spatial evolution of mass-transfer rate is closely correlated with turbulent intensity and local pressure gradients induced by geometric discontinuities of the flow channel. The mass-transfer active zones are consistently concentrated at geometric transition sections, which constitute the core regions for cavitation occurrence in the fuel channel, as illustrated in Figure 10.

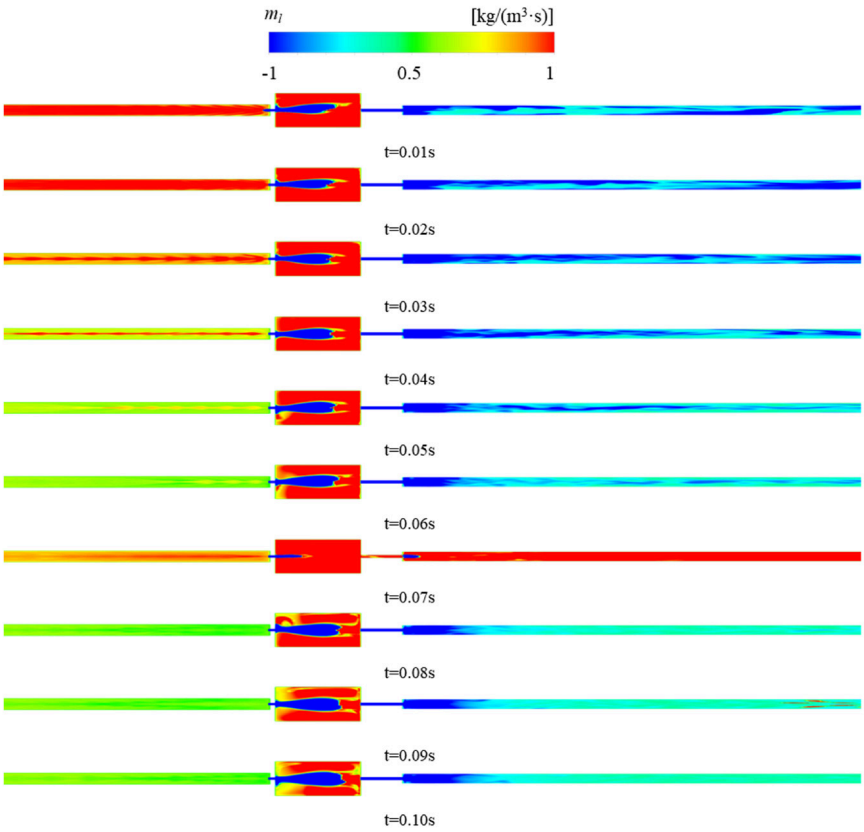


Figure 10. Cloud map of mass-transfer rate with different sizes in the computational domain under the inlet velocity of 4.39 m/s.

4. Conclusions

This study focuses on the fuel passage of high-temperature valves and systematically investigates the steady-state flow field, gas volume fraction distribution, transient gas phase evolution, mass-transfer characteristics and cavitation behavior under three inlet velocities of 0.88 m/s, 2.63 m/s and 4.39 m/s through numerical simulations. The regulation effect of inlet velocity on gas–liquid two-phase flow and cavitation characteristics is clarified. The main conclusions are summarized as follows:

1. Gas volume fraction and bubble size effect: The increase in inlet velocity significantly promotes gas accumulation in the pipeline. Discontinuous gas distribution appears

under high-velocity conditions, exhibiting characteristics of linear cavitation regions. Large-sized bubbles accumulate in the form of central peaks in the constricted section, while small bubbles with a size of 0.010–0.017 mm show a wall peak distribution. The increase in inlet velocity leads to a general rise in gas volume fraction for all bubble groups, and the recovery magnitude of gas volume fraction for the 0.010 mm group increases significantly with rising flow velocity.

2. Transient gas phase and mass-transfer characteristics: Under low inlet velocity, mass transfer follows the evolutionary pattern of low steady state, abrupt change in mass-transfer direction and rapid decline. For medium velocity, the mass-transfer process remains relatively stable and expands toward the inlet section. Under high velocity, a high mass-transfer rate exists from the initial stage, and the active region gradually contracts toward the expanded section, leading to rapid achievement of mass-transfer equilibrium.
3. Cavitation characteristics: A dynamic cycle of gas dissolution, precipitation and re-dissolution exists within the fuel passage. High inlet velocity is a key factor inducing cavitation. The discontinuous gas zone formed under 4.394 m/s is essentially a linear cavitation region caused by local pressure dropping below the saturation pressure, which constitutes a potential risk of gaseous cavitation in practical operation.

The findings of this study provide theoretical support and reference data for the structural optimization, cavitation suppression and operating condition determination of fuel passages. Further research can incorporate experimental verification, and carry out quantitative analysis on temperature coupling, multi-phase flow model modification and wall material effects on cavitation. Meanwhile, long-term erosion damage assessment of cavitation areas can be conducted in subsequent studies.

Author Contributions: Z.R.: Methodology, funding acquisition, writing—original draft, writing—review and editing, software, Z.G.: Writing—review and editing, resources, project administration, Y.Z.: Formal analysis, investigation, Z.Z.: Formal analysis, investigation, Z.J.: Conceptualization, writing—original draft, L.N.: Formal analysis, investigation, project administration, W.Z.: Supervision, validation. All authors have read and agreed to the published version of the manuscript.

Funding: This study was supported by National Natural Science Foundation of China (Grant No. 524B2076, U23B2033) and the Heilongjiang Postdoctoral Fund (LBH-Z25154).

Institutional Review Board Statement: Not applicable.

Informed Consent Statement: Not applicable.

Data Availability Statement: Data supporting the findings of this study are available from the corresponding authors upon reasonable request.

Conflicts of Interest: The authors declare no conflicts of interest.

References

1. Duke, D.J.; Matusik, K.E.; Kastengren, A.L.; Swantek, A.B.; Sovis, N.; Payri, R.; Viera, J.P.; Powell, C.F. X-ray radiography of cavitation in a beryllium alloy nozzle. *Int. J. Engine Res.* **2017**, *18*, 39–50. [CrossRef]
2. Duke, D.J.; Kastengren, A.L.; Swantek, A.B.; Matusik, K.E.; Powell, C.F. X-ray fluorescence measurements of dissolved gas and cavitation. *Exp. Fluids* **2016**, *57*, 162. [CrossRef]
3. Yang, S. Modeling of Diesel Injection in Subcritical and Supercritical Conditions. Ph.D. Thesis, Université Paris-Saclay, Orsay, France, 2019.
4. Iben, U.; Makhnov, A.; Schmidt, A. Numerical study of the effects of dissolved gas release in cavitating flow. *AIP Conf. Proc.* **2018**, *2027*, 030128. [CrossRef]
5. Khozaei, M.H.; Favrel, A.; Miyagawa, K. Influence of swirling flow parameters on frequency response of a simplified draft-tube in presence of cavitation. *Int. J. Heat Fluid Flow* **2022**, *98*, 109043. [CrossRef]

6. Zhou, J.; Vacca, A.; Casoli, P. A novel approach for predicting the operation of external gear pumps under cavitating condi-tions. *Simul. Model. Pract. Theory* **2014**, *45*, 35–49. [CrossRef]
7. Ren, Z.P.; Li, D.Y.; Zhou, W.X.; Liu, J.; Li, Y. Energy distribution and thermodynamic assessment of cavitating coolant flow in a micropump. *Energy* **2025**, *340*, 139261. [CrossRef]
8. Peters, A.; El Moctar, O. Numerical assessment of cavitation-induced erosion using a multi-scale Euler–Lagrange method. *J. Fluid Mech.* **2020**, *894*, A19. [CrossRef]
9. Ali, H.; Solsvik, J. Bubble hydrodynamics and mass transfer in stirred tank with non-Newtonian fluids: Scale-up from labor-atory to pilot-scale. *Phys. Fluids* **2021**, *33*, 033319. [CrossRef]
10. Ren, Z.P.; Li, D.Y.; Zhou, W.X.; Li, Z.; Wang, H.; Liu, J.; Li, Y.; Khoo, B.C. Gas–liquid mass-transfer characteristics during dissolution and evolution in quasi-static and dynamic processes. *Int. J. Multiph. Flow* **2024**, *180*, 104970. [CrossRef]
11. Ren, Z.P.; Li, D.Y.; Fu, X.L.; Wang, H.; Liu, J.; Li, Y. Synergistic effects of vapor and gaseous cavitation and mass-transfer mechanism in a mechanical pump. *Phys. Fluids* **2023**, *35*, 053335. [CrossRef]
12. Kowalski, K.; Pollak, S.; Hussong, J. Experimental investigation of cavitation induced air release. *EPJ Web Conf.* **2017**, *143*, 2054. [CrossRef]
13. Kowalski, K.; Pollak, S.; Skoda, R.; Hussong, J. Experimental study on cavitation-induced air release in orifice flows. *J. Fluids Eng.* **2018**, *140*, 061201. [CrossRef]
14. Li, X.; Chen, G.; Zhang, P.; Wang, W.; Li, J. Quantitative analysis for the effects of internal flow on mass transfer processes inside rising bubbles. *Phys. Fluids* **2019**, *31*, 117107. [CrossRef]
15. Long, S.; Yang, X.; Yang, J.; Sommerfeld, M. Euler/Euler large eddy simulation of bubbly flow in bubble columns under CO_2 chemisorption conditions. *Chem. Eng. J.* **2022**, *445*, 136654. [CrossRef]
16. Huang, Z.; Shuai, Y.; Ren, C.; Yang, Y.; Sun, J.; Wang, J.; Yang, Y. Effects of internal structures on mass transfer performance of jet bubbling reactor. *Chem. Eng. Process.* **2022**, *175*, 108936. [CrossRef]
17. Yan, H.; Gong, H.; Huang, Z.; Zhou, P.; Liu, L. Euler–Euler modeling of reactive bubbly flow in a bubble column. *Phys. Fluids* **2022**, *34*, 053306. [CrossRef]
18. Zhou, Z.; Yuan, Q.; Jia, X.; Feng, W.; Wen, J. Experimental study and CFD simulation of mass transfer characteristics of a gas-induced pulsating flow bubble. *Chem. Biochem. Eng. Q.* **2013**, *2*, 167–175.
19. Daskiran, C.; Liu, I.-H.; Oztekin, A. Computational study of multiphase flows over ventilated translating blades. *Int. J. Heat Mass Transf.* **2017**, *110*, 262–275. [CrossRef]
20. Daskiran, C.; Attiya, B.; Altimemy, M.; Liu, I.-H.; Oztekin, A. Oxygen dissolution via pump-turbine—Application to wastewater treatment. *Int. J. Heat Mass Transf.* **2019**, *131*, 1052–1063. [CrossRef]
21. Ren, Z.P.; Li, D.Y.; Wang, H.J.; Liu, J.; Li, Y. Computational model for predicting the dynamic dissolution and evolution behaviors of gases in liquids. *Phys. Fluids* **2022**, *34*, 103310. [CrossRef]
22. Bastos, F.; Rachid, D.F. Modeling gaseous and vaporous cavitation in liquid flows within the context of the thermodynamics of irreversible processes. *Int. J. Non-Linear Mech.* **2014**, *65*, 245–252. [CrossRef]
23. Da Silva, A.B.; de Freitas Rachid, F.B. Modeling of release and absorption of gas in liquid–gas flows within a consistent thermodynamic framework. *Int. J. Eng. Sci.* **2013**, *66*, 21–43. [CrossRef]
24. Kessal, M.; Bennacer, R. A new gas release model for a homogeneous liquid–gas mixture flow in pipelines. *Int. J. Press. Vessels Pip.* **2005**, *82*, 713–721. [CrossRef]
25. Yin, Z.G.; Zhao, Q.; Cao, X.W. Oxygen transport and diffusion numerical simulation on water and oxygen transport and diffusion numerical simulation on water and air mixture of plug discharge. *Adv. Water Sci.* **2013**, *24*, 410–417.

Disclaimer/Publisher's Note: The statements, opinions and data contained in all publications are solely those of the individual author(s) and contributor(s) and not of MDPI and/or the editor(s). MDPI and/or the editor(s) disclaim responsibility for any injury to people or property resulting from any ideas, methods, instructions or products referred to in the content.